SLC16A3-Induced Lactate Remodeling Drives Immune Evasion in Clear Cell Renal Cell Carcinoma via an Autocrine GPR81-ERK-c-MYC Feedback Loop

Shidong Zuo[1,2], Jinkai Dong[2], Yuhao Dong[1,3], Chengwei Fu[2], Xuechao Li[2], Baobo Zhao[2], Lu Wang[4], Yongjie Zhang[5], Lingsheng Kong[2], Tao Yang[2], Lijun Chen[1,2]

[1]Medical School of Chinese PLA: Chinese PLA General Hospital, Beijing, China
[2]Department of Urology, The Third Medical Center, Chinese PLA General Hospital, Beijing, China
[3]Department of Urology, 982nd Hospital of the Joint Logistics Support Force, Tangshan, China
[4]Department of Obstetrics and Gynecology, The Seventh Medical Center, Chinese PLA General Hospital, Beijing, China
[5]Department of Urology, Peking University People's Hospital, Beijing, China

Background: Extensive studies have implicated glycolytic reprogramming and lactate accumulation in immune evasion. However, clustered regularly interspaced short palindromic repeats (CRISPR)-based *in vivo* screens systematically interrogating metabolic drivers of immune checkpoint blockade resistance in clear cell renal cell carcinoma (ccRCC) remain scarce. Consequently, direct *in vivo* evidence delineating how the lactate exporter solute carrier family 16 member 3 (*SLC16A3*; monocarboxylate transporter 4, MCT4) rewires tumor lactate metabolism to promote immune escape in ccRCC is still lacking.

Aims: To identify key metabolic genes governing immune checkpoint blockade resistance in ccRCC via *in vivo* CRISPR screening, elucidate the molecular mechanisms of *SLC16A3*-mediated lactate reprogramming in regulating glycolysis and immune suppression, and validate the therapeutic potential of MCT4 inhibition combined with anti-programmed cell death protein-1 (anti-PD-1) therapy for ccRCC.

Study Design: Integrated *in vivo* CRISPR screening, functional assays, and clinical validation.

Methods: A metabolic CRISPR library-based screen was conducted in an *in vivo* immunocompetent ccRCC model treated with an anti-PD-1 antibody. Single-guide RNAs (sgRNAs) targeting glycolysis-associated genes were differentially enriched. Analyses of The Cancer Genome Atlas dataset and the Tumor Immune Estimation Resource database were performed, and an institutional tissue microarray analysis assessed survival outcomes. *SLC16A3*-knockout and *SLC16A3*-overexpressing RENCA cells were generated to evaluate tumor growth in immunodeficient and immunocompetent mice, alongside immune cell infiltration profiling. Seahorse metabolic assays, flow cytometry, lactate-treated macrophage assays, and G-protein–coupled receptor 81 (GPR81) antagonism or genetic suppression were used to dissect the lactate export/receptor axis. Additionally, *SLC16A3*-knockdown and *SLC16A3*-overexpressing 786-O and SN12C ccRCC cells were established. RNA sequencing, protein stability, ubiquitination, and phosphorylation analyses were conducted to elucidate the underlying molecular mechanisms.

Results: Anti-PD-1 therapy selectively reduced sgRNA counts for glycolysis–lactate genes, most notably Ldha and *SLC16A3*. While *SLC16A3* depletion modestly restricted intrinsic ccRCC proliferation in immunodeficient models, its predominant effect was remodeling the tumor immune microenvironment. *SLC16A3*-mediated lactate export activated macrophage extracellular signal-regulated kinase (ERK) signaling in a GPR81-dependent manner, promoted M2 macrophage polarization, and suppressed $CD8^+$ T-cell function. Concurrently, exported lactate engaged tumor GPR81 to activate autocrine ERK signaling and phosphorylate c-MYC at Ser62, preventing F-box and WD repeat domain-containing 7-mediated degradation. This stabilized c-MYC upregulated lactate dehydrogenase A, glucose transporter 1, and hypoxia-inducible factor 1 alpha, forming a self-sustaining glycolytic feedback loop

Corresponding author: Lijun Chen, Medical School of Chinese PLA: Chinese PLA General Hospital; Department of Urology, The Third Medical Center, Chinese PLA General Hospital, Beijing, China

e-mail: Chenlijun301@outlook.com

Received: January 26, 2026 **Accepted:** April 2, 2026 • **DOI:** 10.4274/balkanmedj.galenos.2026.2026-1-247

Available at www.balkanmedicaljournal.org

ORCID iDs of the authors: S.Z. 0009-0003-0570-7099; J.D. 0009-0004-9486-2273; Y.D. 0009-0009-2017-6314; C.F 0009-0009-7994-8710; X.L. 0009-0007-7317-1694; B.Z. 0009-0002-4231-4123; L.W. 0009-0000-3384-9594; Y.Z. 0009-0006-5557-1160; L.K. 0009-0008-4137-7644; T.Y. 0009-0007-3572-7049; L.C. 0009-0008-1600-9882.

Cite this article as: Zuo S, Dong J, Dong Y, et al. Solute Carrier Family 16 Member 3 Identified by *In Vivo* Clustered Regularly Interspaced Short Palindromic Repeats Screening Reprograms Glycolysis via the Autocrine Extracellular Signal-Regulated Kinase-c-MYC Axis and Promotes Immune Suppression in Clear Cell Renal Cell Carcinoma. Balkan Med J. [Epub Ahead of Print]

uniquely amplified in the von Hippel–Lindau–deficient background of ccRCC. Clinically, tissue microarray analysis indicated a trend toward worse progression-free survival in patients with high MCT4 expression. Furthermore, combining the MCT4 inhibitor MSC-4381 with PD-1 blockade markedly reduced tumor volume in immunocompetent mice, demonstrating enhanced combinatorial efficacy.

Conclusion: *SLC16A3*-induced lactate reprogramming drives immune resistance in ccRCC via two converging mechanisms: extracellular lactate-mediated immunosuppression through M2 macrophage polarization and an autocrine GPR81–ERK–c-MYC glycolytic feedback loop. These findings highlight MCT4 blockade combined with immune checkpoint inhibition as a rational strategy to overcome immunotherapy resistance.

INTRODUCTION

Renal cell carcinoma (RCC) is a major global malignancy, with the clear cell renal cell carcinoma (ccRCC) notable for its high prevalence and aggressive clinical course.[1,2] The clinical adoption of immune checkpoint blockade (ICB) has transformed frontline oncology; however, its therapeutic efficacy remains limited by intrinsic and acquired resistance mechanisms, with long-term response rates below 20%.[3-5]

Specifically, over 60% of patients with ccRCC fail to respond to single-agent immune checkpoint inhibitors, and acquired resistance eventually develops in nearly all cases treated with targeted combination regimens.[6] Extensive studies have identified contributing factors, including T-cell exhaustion,[7,8] defects in antigen presentation,[9,10] and the establishment of an immunosuppressive tumor microenvironment (TME).[11,12] Despite this progress, the precise metabolic vulnerabilities that dictate therapeutic failure remain incompletely understood.

To systematically decode the metabolic dependencies underlying ICB resistance, we performed a metabolism-focused *in vivo* clustered regularly interspaced short palindromic repeats–CRISPR-associated protein 9 (CRISPR-Cas9) screen. CRISPR-Cas9 utilizes RNA-guided endonucleases to induce site-specific DNA cleavage, enabling genome-wide functional interrogation.[13] While *in vitro* screening offers technical simplicity and requires fewer cells for initial candidate discovery,[14] it lacks native immune components, preventing assessment of immune effector dynamics and inter-organ crosstalk.[15] In contrast, *in vivo* models preserve immune network integrity and vascular barriers, accurately recapitulating the clonal survival pressures that drive clinical resistance.[16] The physiological relevance of such models demands highly infection-efficient systems, increasing technical complexity and resource requirements.[17] Accordingly, we conducted a metabolism-focused CRISPR knockout screen in an immunocompetent ccRCC model to systematically interrogate which metabolic pathway genes govern resistance to ICB.

Aerobic glycolysis, classically recognized as the Warburg effect, promotes substantial lactate accumulation within neoplastic tissues, where lactate functions as a key signaling mediator. It drives the polarization of tumor-associated macrophages (TAMs) toward an M2-like phenotype, thereby impeding cytotoxic $CD8^+$ T-cell infiltration.[18] Moreover, lactate induces histone H3 lysine 18 lactylation in myeloid cells, epigenetically enhancing programmed death-ligand 1 (PD-L1) expression and establishing a potent metabolic barrier against anti-programmed cell death protein-1 (anti-PD-1) therapy.[19] At the molecular level, engagement of the lactate receptor G-protein-coupled receptor 81 (GPR81) activates the mitogen-activated protein kinase (MAPK) signaling cascade, promoting expansion of regulatory T-cells (Tregs) and myeloid-derived suppressor cells (MDSCs), while simultaneously attenuating natural killer cell degranulation.[20,21]

Although metabolic reprogramming—particularly glycolysis and lactate accumulation—has been increasingly implicated in immune evasion, the mechanisms by which solute carrier family 16 member 3 (*SLC16A3*), encoding the monocarboxylate transporter 4 (MCT4), regulates tumor glycolysis and immune escape in ccRCC remain incompletely understood and require further investigation.

Intracellular metabolic flux is tightly regulated by the solute carrier (SLC) superfamily.[22] Among its members, *SLC16A3* encodes the principal cytosolic lactate exporter, MCT4, acting as a crucial determinant of glycolytic output and systemic lactate homeostasis.[23] Previous studies have shown that the liver kinase B1 (LKB1)–MCT4 axis modulates pericellular lactate gradients, directing macrophage polarization and impairing antitumor immunosurveillance.[24] In ccRCC, *SLC16A3* transcripts are markedly enriched under diverse metabolic stresses, serving as a key determinant of the tumor immunogenic profile.[25] However, direct *in vivo* evidence demonstrating how *SLC16A3* coordinates autocrine metabolic reprogramming with immune evasion in ccRCC remains limited.

MATERIALS AND METHODS

Cell culture

Murine (RENCA, RAW264.7) and human (786-O, SN12C) cell lines were obtained from Procell (China). RENCA and 786-O cells were cultured in Roswell Park Memorial Institute-1640 medium, whereas RAW264.7 and SN12C cells were maintained in Dulbecco's Modified Eagle Medium. All media were supplemented with 10% fetal bovine serum (Procell, 164210) and 1% penicillin-streptomycin (Biosharp, BL505A). For RENCA cultures, 1 mM sodium pyruvate (Biosharp, BL1277A) and 1% non-essential amino acids (Biosharp, BL1115A) were additionally included. Cells were incubated in a humidified atmosphere containing 5% CO_2 at 37 °C.

Ethics and informed consent

All animal procedures in this study were approved by the Institutional Animal Care and Use Committee of the Chinese PLA General Hospital, and were conducted in strict accordance with the National Institutes of Health Guide for the Care and Use of Laboratory Animals.

The human tissue microarray research protocol was approved by the Ethics Committee of The Fifth Medical Center of Chinese People's Liberation Army General Hospital (approval number: KY-2022-6-40-1, date: 16.06.2022). Written informed consent, which permits the future use of surplus biological material and anonymized clinical information for research purposes, was obtained from each participant enrolled in the tissue microarray cohort.

CRISPR screening for metabolic regulators of PD-1 blockade resistance

Metabolic CRISPR screening was performed using a mouse metabolic CRISPR library (HyCyte, #163966; 18,342 single-guide RNAs (sgRNAs) targeting 2,918 genes; 6 sgRNAs per gene; 100 non-targeting controls). Due to the low lentiviral permissiveness of RENCA cells, the library was delivered at a high physical multiplicity of infection (MOI) of 30. Following a 3-day selection with puromycin (0.5 μg/mL), the surviving fraction was 12.87%. Based on the Poisson distribution [$P(k) = e^{(-m)}m^k / k!$, where m is the effective MOI], this corresponds to a functional MOI of 0.138, ensuring single-copy sgRNA integration in > 93% of transduced cells. To maintain 300-fold library coverage and avoid *in vivo* bottlenecks, 5.55×10^6 surviving cells were subcutaneously inoculated into 4-week-old female BALB/c mice (n = 3 per group).

Three days post-inoculation, mice received three intraperitoneal doses (100 μg each) of either murine anti-PD-1 monoclonal antibody (RMP1-14; BioXcell) or IgG2a isotype control (BE0089; BioXcell) at three-day intervals. Tumors were harvested on Day 12, and genomic DNA was extracted for sgRNA amplification and sequencing (Illumina NovaSeq). Raw read counts were normalized using median normalization within the MAGeCK framework. Biological variability among replicates (n = 3 per group) was modeled using MAGeCK's negative binomial distribution. Hits were defined as $|\log_2 \text{fold change}| \geq 1$ with adjusted $p < 0.05$ (MAGeCK-robust rank aggregation/MLE). Gene set enrichment analysis (MAGeCK-Flute) identified metabolic pathways associated with PD-1 blockade resistance. All *in vivo* screening experiments included all mice in the final analysis without exclusions.

In vivo experiments in mice

All animal procedures were approved by the Institutional Animal Care and Use Committee of the Chinese PLA General Hospital and were conducted in accordance with the National Institutes of Health Guide for the Care and Use of Laboratory Animals.

Tumor-intrinsic growth assay in immunodeficient mice: Female BALB/c nude mice (4 weeks old) were randomly assigned to experimental groups (n = 7 per group). Tumors were established via subcutaneous injection of 5×10^5 RENCA cells in 100 μL of sterile phosphate-buffered saline (PBS) into the right flank. Mice were sacrificed on Day 16, and tumors were collected for subsequent analyses.

Anti-PD-1 efficacy assay in immunocompetent mice: Female BALB/c mice (4 weeks old) were randomized into groups (n = 5 per group). Tumors were induced via subcutaneous injection of 5×10^5 RENCA cells in 100 μL of PBS. On Days 7, 10, and 13 post-inoculation, 100 μg of murine anti-PD-1 antibody (BioXcell, RMP1-14) or immunoglobulin G2a (IgG2a) isotype control (BioXcell, BE0089) was administered intraperitoneally. Mice were sacrificed on Day 16, and tumors were harvested for flow cytometry and further analyses.

MCT4 inhibitor and anti-PD-1 combination therapy assay: Female BALB/c mice (4 weeks old) were randomized into groups (n = 5 per group). Tumors were induced via subcutaneous injection of 5×10^5 RENCA cells in 100 μL of PBS. Beginning on Day 7, mice received intraperitoneal injections of 600 μg MSC-4381 (MCT4 inhibitor; MCE, HY-132301) until the end of the experiment. An anti-PD-1 antibody or isotype control was administered on Days 7, 10, and 13. Mice were sacrificed on Day 16, and tumors were harvested for volumetric measurement and further analyses.

Randomization and blinding: Upon arrival, all mice were marked with unique ear tags and randomly assigned to experimental groups using a computer-generated random number table, ensuring balanced baseline characteristics. Group assignments were completed prior to tumor cell inoculation, and no re-randomization was performed. Blinded outcome assessment was not implemented, as the same researcher conducted tumor cell preparation, animal inoculation, drug administration, and tumor volume measurements. No animals or data points were excluded from analysis. Future studies will separate personnel responsible for experimental design, cell culture, and drug preparation from those performing animal operations and outcome measurements to enable blinded assessment.

In vivo tumor assays

Tumor growth in immunodeficient mice: Female BALB/c nude mice (4 weeks old) were used to assess *in vivo* tumor proliferation. Tumors were established via subcutaneous injection of 5×10^5 RENCA cells suspended in 100 μL PBS. Mice were sacrificed on Day 16, and tumors were harvested.

Tumor growth in immunocompetent mice: Female BALB/c mice (4 weeks old) were used to evaluate tumor growth in an intact immune environment. Tumors were established as described above. On Days 7, 10, and 13 post-inoculation, 100 μg of murine PD-1 antibody (BioXcell, RMP1-14) or IgG2a isotype control antibody (BioXcell, BE0089) was administered intraperitoneally. Mice were sacrificed on Day 16, and tumors were collected.

Combination therapy with MCT4 inhibitor and anti-PD-1: Female BALB/c mice (4 weeks old) received subcutaneous injections of 5×10^5 RENCA cells in 100 μL PBS. Starting on Day 7, 600 μg of MSC-4381 (MCT4 inhibitor; MCE, HY-132301) was administered intraperitoneally once daily until the study endpoint. Anti-PD-1 antibody or isotype control was administered as described above.

Flow cytometry analysis

Cells were stained with the following antibodies: Brilliant Violet 510 anti-mouse CD45 (BioLegend, 103138), PerCP/Cyanine5.5 anti-mouse CD3 (BioLegend, 100218), PE/Cyanine7 anti-mouse CD4 (BioLegend, 100422), Brilliant Violet 421 anti-mouse CD25 (BioLegend, 102033),

Foxp3/Transcription Factor Staining Buffer Set (eBioscience, 00-5523-00), Brilliant Violet 605 anti-mouse CD8a (BioLegend, 100744), FITC anti-human/mouse granzyme B recombinant (BioLegend, 372206), APC/Fire 750 anti-mouse CD223 (LAG-3; BioLegend, 125240), APC anti-mouse CD366 (Tim-3; BioLegend, 134008), FITC anti-mouse F4/80 (BioLegend, 123107), APC/Cyanine7 anti-mouse/human CD11b (BioLegend, 101226), PE anti-mouse CD86 (BioLegend, 105007), and APC anti-mouse CD206 (MMR; BioLegend, 141708).

Colony formation and CCK-8 assays

Colony formation assay: RENCA cells with varying *SLC16A3* expression were seeded at 700 cells per well in six-well plates containing 2 mL of medium. The medium was replaced every 2 days. After 14 days, cells were fixed with 4% paraformaldehyde and stained with crystal violet.

CCK-8 assay: RENCA cells were seeded at 3,000 cells per well in 96-well plates containing 200 µL of medium. Cell proliferation was measured at 0, 24, 48, and 72 hours using the CCK-8 kit (EallBio, 03.S17002DA).

Plasmid and siRNA transfection

Gene targets and sequences:

Mouse *SLC16A3*: sg-1: AAAAGACGCTGACCGCCTTG; sg-2: TATGGGTGTACCCGACACAA

Human *SLC16A3*: sh1: CGTCTACATGTACGTGTTCAT; sh2: GCTCATACAGGAGTTTGGGAT

Mouse *Gpr81*: si-1: CATCTTGTTCTGCTCGGTCAA; si-2: CCTCTGGACTTTGGTCATCTT

Human *GPR81*: si-1: CGTGTCTGCTAGACTCTATTT; si-2: GTGTGGTTTCTGCTTCCACAT

Transfections were performed using Lipofectamine 3000 (ThermoFisher, L3000015) according to the manufacturer's instructions.

Western blot analysis

Western blotting and immunofluorescence were performed as previously described.[26] The primary antibodies used included MCT4 (Proteintech, 22787-1-AP), phospho-extracellular signal-regulated kinase (ERK) (p-ERK, Proteintech, 28733-1-AP), ERK (Proteintech, 28733-1-AP), (phospho-signal transducer and activator of transcription 1, CST, 9167T), STAT1 (Proteintech, 10144-2-AP), GPR81 (Proteintech, 20146-1-AP), c-MYC (Proteintech, 10828-1-AP), phospho-c-MYC Ser62 (p-c-MYC S62, CST, 13748T), hypoxia-inducible factor 1 alpha (HIF1α; Proteintech, 20960-1-AP), glucose transporter 1 (GLUT1) (Proteintech, 21829-1-AP), lactate dehydrogenase A (LDHA) (Proteintech, 19987-1-AP), FLAG tag (Proteintech, 80801-2-RR/66008-4-Ig), HA tag (Proteintech, 51064-2-AP/66006-2-Ig), and β-ACTIN (Proteintech, 66009-1-Ig). Protein detection was performed using BeyoECL Plus (P0018S) and analyzed with Image Lab 3.0 (Bio-Rad Laboratories, Inc.).

Co-immunoprecipitation experiment

Stably transfected 786-O cells were generated by co-transfecting ubiquitin-HA and c-MYC-FLAG overexpression (OE) plasmids. One group of cells was treated with 20 mM L-lactate, while the control group was cultured in standard medium. After 48 hours, cells were incubated with 20 µM MG132 for 6 hours, and cell lysates were harvested.

The c-MYC-FLAG protein was purified using FLAG magnetic beads (MCE, HY-K0207). Eluted samples were subjected to Western blot analysis, with ubiquitin detected using an HA antibody, and c-MYC visualized using a FLAG antibody.

Immunohistochemistry and evaluation

Tissue microarray sections were stained for MCT4 (Proteintech, 22787-1-AP) following standard immunohistochemistry (IHC) protocols. Protein expression was evaluated semi-quantitatively by two independent pathologists blinded to clinical data. Staining intensity was scored as 0 (negative), 1 (weak), 2 (moderate), or 3 (strong), and the percentage of positive cells was scored as 0 (0%), 1 (1-25%), 2 (26-50%), 3 (51-75%), or 4 (76-100%). A final staining index, ranging from 0 to 12, was calculated by multiplying the intensity and percentage scores. For survival analysis, patients were stratified using the median staining index as a predefined cut-off; values above the median were classified as high MCT4 expression, and values at or below the median were classified as low expression.

Statistical analysis

Statistical analyses were performed using GraphPad Prism software. For cross-sectional data involving comparisons among three or more groups, one-way analysis of variance (ANOVA) was conducted, followed by Tukey's test for all pairwise comparisons or Dunnett's test for comparisons against a single control to control the family-wise error rate. For pathway-level enrichment and high-throughput transcriptomic analyses, the false discovery rate was controlled using the Benjamini-Hochberg procedure. Longitudinal tumor growth data with potential missing values, such as those arising from variable tumor engraftment or animal mortality, were analyzed using a linear mixed-effects model implemented via restricted maximum likelihood. For balanced longitudinal data without missing values, two-way repeated-measures (RM) ANOVA was applied, with time and treatment group as factors; the Geisser-Greenhouse correction was used to address violations of sphericity. Post-hoc comparisons of tumor volumes at specific time points or at the experimental endpoint were performed using Tukey's multiple comparisons test. Data are presented as mean ± standard deviation, and adjusted p values less than 0.05 were considered statistically significant. Exact p values, including non-significant trends, were explicitly reported.

RESULTS

CRISPR library reveals glycolysis and lactate metabolism as critical drivers of immune resistance in renal cell carcinoma

The experimental schematic is shown in Figure 1a. Stable RENCA cell lines were generated using a CRISPR library targeting the mouse metabolome. Female BALB/c mice were inoculated subcutaneously with these cells to establish tumors and subsequently randomized into two groups. Anti-IgG2a and anti-PD-1 antibodies (BioXcell) were administered intraperitoneally starting on Day 3 post-inoculation, with injections repeated every three days for a total of three doses (Figure 1a).

Next-generation sequencing revealed significant alterations in sgRNA representation targeting glycolytic metabolic pathways. Among the top ten differentially represented targets, key glycolysis-related genes, including *Ldha* and *SLC16A3*, were prominently enriched (Figure 1b). A gene set of glycolysis-associated genes—including *Glut1*, *Hif1a*, *Hk2*, *Ldha*, *SLC16A3*, and others—was constructed. Gene set enrichment analysis demonstrated a significant association between this glycolysis-related gene signature and response to PD-1 blockade (Figure 1c). Using the Tumor Immune Estimation Resource (TIMER) database, we observed that *SLC16A3* expression levels were significantly correlated with M2 macrophage infiltration in ccRCC (Figure 1d). Analysis of The Cancer Genome Atlas dataset indicated that *SLC16A3* is broadly upregulated across multiple tumor types, with the most pronounced OE observed in ccRCC compared with adjacent normal tissues (Figure 1e).

SLC16A3 dictates the response to PD-1 blockade in immunocompetent microenvironments rather than serving solely as an intrinsic proliferation driver

We next investigated the functional role of *SLC16A3* in RCC. Stable *SLC16A3* knockout and overexpressing RENCA cell lines were established. Western blot analysis confirmed successful modulation of *SLC16A3* (MCT4) protein expression *in vitro* (Figure 2a). Neither knockout nor OE of *SLC16A3* significantly affected colony formation or cell proliferation in RENCA cells under standard *in vitro* culture conditions (Figure 2b).

To evaluate tumor-intrinsic growth *in vivo*, subcutaneous tumor assays were performed in immunodeficient nude mice, which lack mature T-cells. Longitudinal analysis of tumor growth kinetics showed that *SLC16A3* knockout induced a statistically significant but modest reduction in tumor progression compared with the control group (two-way RM ANOVA, interaction effect $p = 0.0002$ [$F(4, 48) = 6.769$]; main effect of group $p = 0.0401$ [$F(1, 12) = 5.298$]. At the experimental endpoint (Day 16), the mean tumor volume in the knockout group was reduced by 115.7 mm³ (adjusted $p < 0.0001$, Tukey's multiple comparisons test), yielding a tumor growth inhibition (TGI) of 16.53% (Figure 2c).

Conversely, *SLC16A3* OE did not significantly affect either the longitudinal growth trajectory (two-way RM ANOVA with Geisser-Greenhouse correction, interaction effect $p = 0.5076$; main effect of group $p = 0.9108$) or the endpoint tumor volume (adjusted $p = 0.9976$) (Figure 2d).

Importantly, the biological impact of *SLC16A3* was markedly amplified in immunocompetent BALB/c mice, fundamentally determining the therapeutic efficacy of PD-1 blockade. Longitudinal tumor growth data, analyzed using a linear mixed-effects model with restricted maximum likelihood, revealed highly significant effects for both the time × group interaction [$p < 0.0001$, $F(5.514, 32.81) = 11.36$] and the group main effect [$p < 0.0001$, $F(5, 119) = 41.56$] (Figure 2e). In the wild-type background, anti-PD-1 monotherapy exhibited strong biological activity, reducing the mean endpoint tumor volume from 664.6 mm³ (negative control, IgG2a) to 271.3 mm³ (anti-PD-1), corresponding to a baseline TGI of 59.18%.

When anti-PD-1 therapy was combined with *SLC16A3* knockout (sg-*SLC16A3* + anti-PD-1), antitumor efficacy was markedly enhanced, resulting in an absolute TGI of 84.14% compared with the baseline control. Conversely, *SLC16A3* OE (OE-*SLC16A3* + anti-PD-1) completely abolished the therapeutic effect of PD-1 blockade, with tumors exhibiting rapid, immune-refractory growth trajectories that were statistically indistinguishable from their isotype-treated counterparts (OE-*SLC16A3* + IgG2a).

Collectively, these data highlight a stark functional contrast: the 16.53% intrinsic growth inhibition observed in immunodeficient mice is vastly overshadowed by the 84.14% combinatorial tumor suppression achieved in the immunocompetent microenvironment. This indicates that, while endogenous *SLC16A3* provides minor metabolic support for autonomous proliferation, its predominant pathophysiological role in ccRCC is to establish an immunosuppressive niche that drives resistance to ICB.

SLC16A3 exports lactate and mediates immunosuppression in the tumor microenvironment via M2 polarization of macrophages

Flow cytometric analysis of subcutaneous tumors in immunocompetent BALB/c mice revealed that changes in *SLC16A3* expression significantly altered tumor-infiltrating immune cell populations, including $CD8^+$ T-cells and their functional states. Specifically, $CD8^+$ T-cell subsets were evaluated using the cytotoxicity marker granzyme B and the exhaustion markers TIM-3 and LAG-3. These changes, together with shifts in macrophage polarization (M1 and M2 subsets), indicate that *SLC16A3* profoundly modulates both effector function and exhaustion status within the tumor immune microenvironment (Figure 3a).

Previous studies by Qian et al.[24] reported that, in lung adenocarcinoma, LKB1 suppresses MCT4 expression; consequently, LKB1 depletion elevates MCT4, enhances lactate export, and generates a high-lactate microenvironment in which lactic acid promotes M2 polarization through engagement of the macrophage receptor Gpr81. We investigated whether a similar MCT4–Gpr81 axis operates in ccRCC. In RENCA, 786-O, and SN12C cells, genetic perturbation of *SLC16A3* markedly reduced the extracellular acidification rate (Figure 3b), confirming that this lactate exporter critically drives glycolytic flux in RCC. This dependency was observed

in both von Hippel–Lindau (VHL) wild-type and VHL-mutant backgrounds, indicating that *SLC16A3*-mediated lactate efflux represents a conserved metabolic vulnerability of ccRCC.

Conditioned medium from RENCA cells stably transfected with either an empty vector (pCDH negative control, NC) or *SLC16A3* OE construct as well as direct treatment of RAW264.7 macrophages (control or siGpr81) with 20 mM L-lactate—a concentration validated to physiologically model the lactate-enriched TME[24]—or the Gpr81 inhibitor 3-OBA, demonstrated that both lactate and tumor cell supernatant, particularly from the OE group, promoted M2 polarization. This was evidenced by an increased proportion of

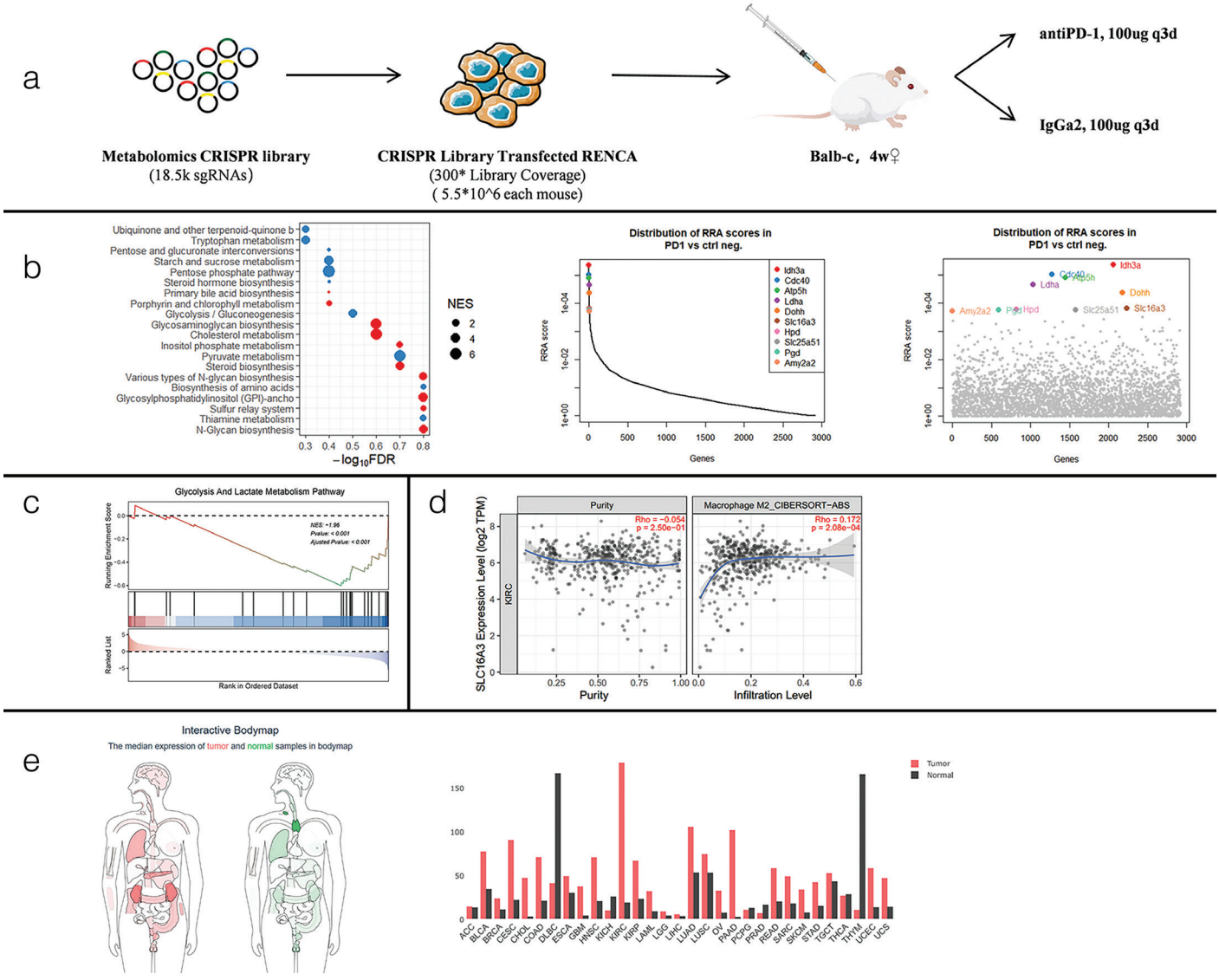

FIG. 1. Clustered regularly interspaced short palindromic repeats (CRISPR) library reveals that glycolysis and lactate metabolism may play a critical role in immune resistance in renal cell carcinoma. Construction of a CRISPR library from the mouse metabolome and stable transfection of RENCA into cell lines (n = 3 per group) (a); next-generation sequencing analysis of mouse tumor tissues following the screen. Left panel: bubble plot illustrating the top enriched metabolic pathways determined by gene set enrichment analysis (GSEA). Bubble size corresponds to the normalized enrichment score, and the x-axis represents the statistical significance ($-\log_{10}$ false discovery rate). Middle and right panels: distribution curves and scatter plots of robust rank aggregation scores for the screened genes [anti-programmed cell death protein-1 (anti-PD-1) vs. immunoglobulin G2a (IgG2a) control] calculated using the MAGeCK algorithm. Key metabolic targets, including SLC16A3 and Ldha, are explicitly highlighted (b); GSEA of a glycolysis and lactate metabolism associated gene signature (c); TIMER analysis revealed a significant correlation between solute carrier family 16 member 3 (SLC16A3) expression levels and M2-polarized macrophage infiltration in clear cell renal cell carcinoma (d); pan-cancer analysis of SLC16A3 mRNA expression levels across various tumor types and matched normal tissues, generated based on the The Cancer Genome Atlas database utilizing the Gene Expression Profiling Interactive Analysis platform (e).

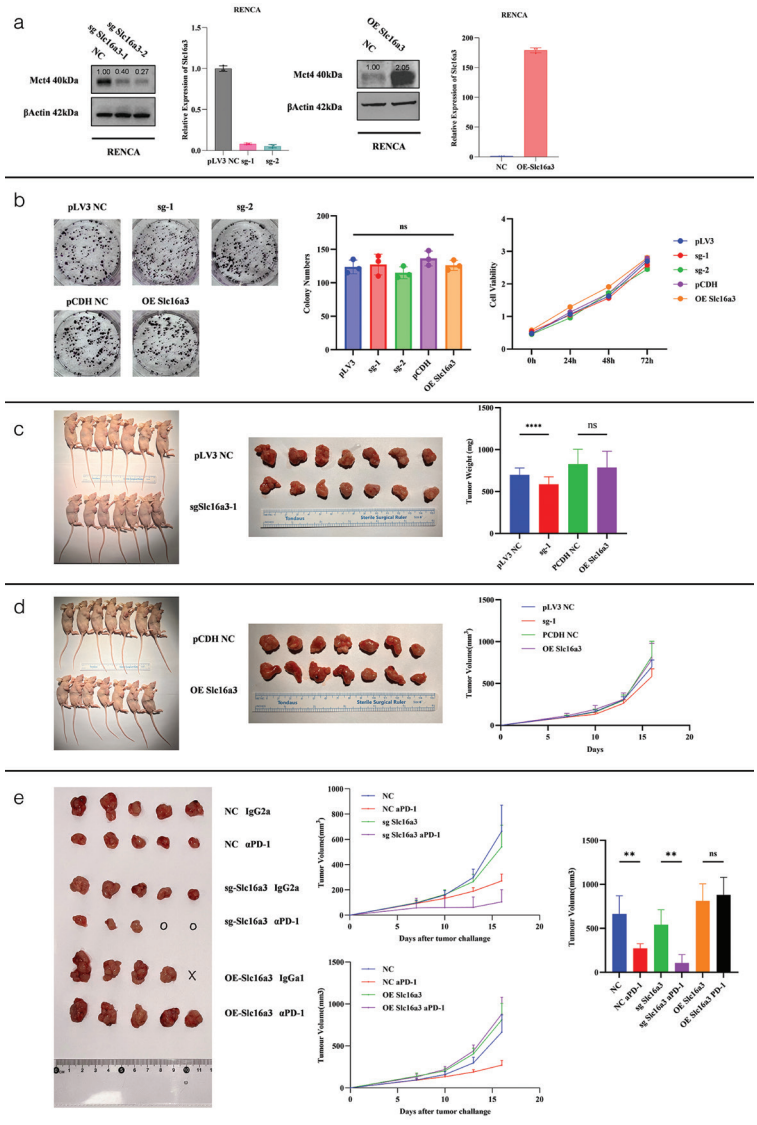

FIG. 2. SLC16A3 dictates the response to programmed cell death protein-1 (PD-1) blockade in immunocompetent microenvironments rather than serving solely as an intrinsic proliferation driver. Stable SLC16A3-knockout and SLC16A3-overexpressing RENCA cell lines were generated, and SLC16A3 [monocarboxylate transporter 4 (MCT4)] protein expression was assessed (a). *In vitro* proliferation and clonogenic capacity of RENCA cells following SLC16A3 knockout or overexpression. For the colony formation assay, cells were seeded in 6-well plates at a density of 700 cells/well and cultured for 14 days before crystal violet staining (left panel). For the Cell Counting Kit-8 (CCK-8) proliferation assay, cells were seeded in 96-well plates at a density of 3000 cells/well, and cellular viability was measured continuously over 72 hours (right panel). Data are presented as mean ± standard deviation (SD) of three independent biological replicates (n = 3 per group). Statistical significance was determined using two-way repeated-measures analysis of variance (ANOVA) for the CCK-8 assay. (b); *in vivo* subcutaneous tumor formation assays in 4-week-old immunodeficient BALB/c nude mice. RENCA cells stably transfected with (c) pLV3 negative control (NC) or sgSLC16A3-1 (knockout), and (d) pCDH NC or overexpression (OE) SLC16A3 (overexpression) were subcutaneously inoculated (n = 7 per group). Tumor volumes were monitored and calculated at Days 7, 10, 13, and 16 post-inoculation. On Day 16, the mice were euthanized, and the excised tumor tissues were photographed and weighed. Statistical significance for longitudinal tumor volumes was determined using two-way repeated-measures ANOVA with Time and Treatment Group as factors, followed by Tukey's multiple comparisons test. The analysis demonstrates that neither the knockout nor the overexpression of SLC16A3 significantly altered the intrinsic *in vivo* proliferation of RENCA cells in the absence of an adaptive immune system (c, d); *in vivo* tumor growth evaluation in immunocompetent BALB/c mice. Mice were subcutaneously inoculated with RENCA cells (NC, sg-SLC16A3, or OE-SLC16A3) and subsequently treated with either immunoglobulin G2a (IgG2a) isotype control or anti-PD-1 antibody. Left: Representative images of excised subcutaneous tumors harvested at the experimental endpoint (Day 16). Middle: Longitudinal tumor growth curves measured over 16 days. Right: Quantification of final tumor weights at Day 16. Data are presented as mean ± SD (n = 5 per group). Statistical significance for longitudinal tumor volume trajectories was determined using a linear mixed-effects model followed by Tukey's post-hoc test. Statistical significance for endpoint tumor weights was evaluated using one-way ANOVA followed by Tukey's multiple comparisons test (e).

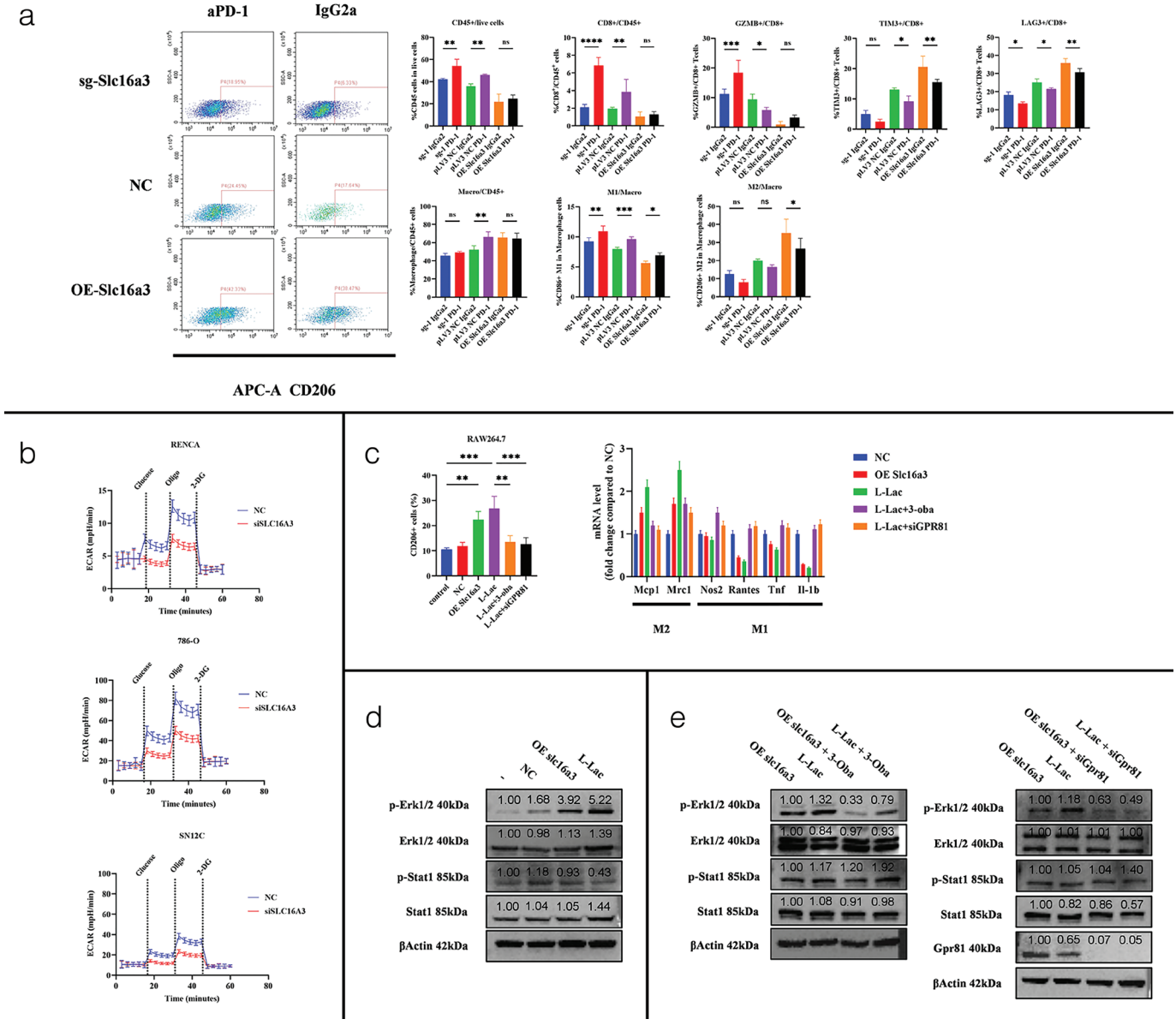

FIG. 3. SLC16A3 exports lactate and mediates immunosuppression in the tumor microenvironment via M2 polarization of macrophages. Flow cytometry analysis of tumor-infiltrating immune cells from subcutaneous tumor models established in immunocompetent BALB/c mice. The panels illustrate the phenotypic characterization of $CD8^+$ T-cells and tumor-associated macrophages (TAMs) within the tumor microenvironment. Specifically, the expression levels of Tim-3 and Lag-3 were evaluated to assess the exhaustion phenotype of $CD8^+$ T-cells, while Granzyme B expression was measured to indicate their cytotoxic capacity. Additionally, the polarization status of TAMs was determined by assessing the expression of CD86 (indicating M1-like polarization) and CD206 (indicating M2-like polarization) (a); measurement of the extracellular acidification rate (ECAR) in RENCA, 786-O, and SN12C cell lines following the interference of solute carrier family 16 member 3 expression. The real-time ECAR was continuously monitored to evaluate the glycolytic flux. Sequential injections of glucose, oligomycin, and 2-deoxy-D-glucose (2-DG) were administered at indicated time points to respectively determine the basal glycolysis, glycolytic capacity, and non-glycolytic acidification of the cells (b); evaluation of macrophage polarization in RAW264.7 cells treated with standard medium (control), conditioned medium (CM) from negative control (NC) or OE-SLC16A3 RENCA cells, and exogenous L-lactate with or without Gpr81 pharmacological inhibition (3-OBA) or genetic silencing (siGpr81). Flow cytometric quantification of the CD206+ (M2) macrophage ratio is shown alongside quantitative real-time PCR analysis of relative mRNA expression levels for M2 markers (Mcp1, Mrc1) and M1 markers (Nos2, Rantes, Tnf, Il1b) (c); western blot analysis of Gpr81, phosphorylated and total extracellular signal-regulated kinase (ERK)1/2, and phosphorylated and total Stat1 in RAW264.7 macrophages subjected to standard medium (control), CM from NC or OE-SLC16A3 RENCA cells, or exogenous 20 mM L-lactate (d); Western blot analysis evaluating the impact of Gpr81 pharmacological inhibition (3-OBA) or genetic silencing (siGpr81) on ERK/Stat1 phosphorylation in RAW264.7 macrophages exposed to OE-SLC16A3 CM or L-lactate (e). ERK, extracellular signal-regulated kinase; OE, overexpression; PD-1, death protein-1; IgG2a, immunoglobulin G2a.

$CD206^+$ macrophages as measured by flow cytometry. This effect was abrogated by Gpr81 inhibition via 3-OBA or small interfering RNA (siRNA)-mediated Gpr81 knockdown (Figure 3c). Similarly, PCR analysis revealed that conditioned medium from *SLC16A3*-overexpressing RENCA cells or L-lactate treatment induced the expression of M2 markers (Mcp1 and Mrc1) and suppressed M1 markers (Nos2, Rantes, Tnf, and Il-1β) in RAW264.7 macrophages (Figure 3c). These effects were reversed by Gpr81 blockade or silencing. At the protein level, *SLC16A3* upregulation and exogenous L-lactate selectively increased ERK11/2 phosphorylation without appreciably altering STAT1 phosphorylation in macrophages (Figure 3d). These signaling activations were similarly attenuated by 3-OBA or siGpr81 (Figure 3e).

Collectively, these results indicate that *SLC16A3* promotes lactate export, creating a high-lactate microenvironment that drives M2 macrophage polarization via the MAPK/STAT signaling axis mediated through Gpr81, thereby contributing to an immunosuppressive TME.

SLC16A3-mediated lactate efflux sustains glycolysis via autocrine ERK–c-MYC signaling

To elucidate the mechanism by which *SLC16A3* promotes immunosuppression in RCC, we established stable 786-O cell lines with either *SLC16A3* OE or siRNA-mediated *SLC16A3* knockdown (Figure 4a). Western blot analysis confirmed successful upregulation of *SLC16A3* (MCT4) in the OE group and downregulation in the knockdown group (Figure 4a).

RNA sequencing revealed that *SLC16A3* knockdown suppressed the MAPK signaling pathway in tumor cells. Given that p-ERK, a key marker associated with M2 macrophage polarization in RAW264.7 macrophages, is part of the MAPK cascade, we hypothesized that lactate exported by *SLC16A3* may exert autocrine effects within tumor cells, leading to ERK phosphorylation and downstream signaling activation (Figure 4b).

A study by Tsai et al.[27] demonstrated that phosphorylation of c-MYC at serine 62 (Ser62) by ERK prevents subsequent phosphorylation at threonine 58 (Thr58) by glycogen synthase kinase-3β. Because phospho-Thr58 serves as the docking residue recognized by the ubiquitin ligase F-box and WD repeat domain-containing 7 (FBW7), ERK-mediated Ser62 phosphorylation prevents FBW7 recruitment, thereby stabilizing c-MYC by shielding it from ubiquitin-dependent proteasomal degradation. Based on these data, we hypothesized that, in RCC, abundant lactic acid sustains c-MYC stability through ERK activation, propagating downstream oncogenic programs beyond immediate metabolic reprogramming. Consistent with this hypothesis, both *SLC16A3* OE and exogenous lactate treatment increased ERK phosphorylation in 786-O and SN12C cells, which further induced c-MYC Ser62 phosphorylation. These effects were reversed by the GPR81 inhibitor 3-OBA or siRNA-mediated GPR81 knockdown (Figure 4c). Similarly, lactate-induced phosphorylation of ERK and c-MYC-Ser62 was abolished by the ERK inhibitor SCH772984 (Figure 4d). Because c-MYC governs the transcription of multiple glycolytic genes—including LDHA, GLUT1, and HIF1A—we quantified their mRNA and protein levels following *SLC16A3* OE or exogenous lactate supplementation. Both interventions elevated LDHA, GLUT1, and HIF1A transcripts in 786-O cells, whereas in SN12C cells, only LDHA and GLUT1 were induced. These effects were reversed by ERK inhibition, supporting the existence of a lactate–GPR81–ERK–c-MYC–glycolytic gene regulatory axis in ccRCC. The differential response between 786-O and SN12C cells likely reflects cell line-specific VHL status, as VHL regulates HIF1α ubiquitination and steady-state levels (Figure 4e).

Furthermore, lactate treatment prolonged the half-life of c-MYC protein in 786-O and SN12C cells (Figure 4f) and attenuated its ubiquitination-mediated degradation (Figure 4g). Mechanistically, this stabilization was mediated through ERK-driven phosphorylation of c-MYC at Ser62.

In summary, these data demonstrate that *SLC16A3*-mediated lactate export engages a tumor-autonomous MAPK–c-MYC signaling axis via autocrine mechanisms, sustaining high glycolytic activity and promoting immunosuppression in ccRCC.

MCT4 inhibition enhances the antitumor effect of PD-1 blockade

To evaluate the clinical prognostic value of MCT4 in ccRCC, IHC analysis was performed on an institutional tissue microarray cohort comprising 91 advanced ccRCC patients, including 41 progression events (Figure 5a). Kaplan–Meier survival analysis indicated a trend toward shorter progression-free survival in patients with high MCT4 expression. To rigorously assess its independent prognostic value and adjust for potential confounding factors, a multivariate Cox proportional hazards regression model was applied. After controlling for basic clinicopathologic variables, including patient age and sex, high MCT4 expression was confirmed as an independent risk factor for poor progression-free survival (hazard ratio = 1.852, 95% confidence interval: 1.016–3.375, $p = 0.0444$; Figure 5b).

In immunocompetent BALB/c mice bearing RENCA subcutaneous tumors, treatment with anti-PD-1 monoclonal antibody significantly suppressed tumor growth compared with the IgG2a isotype control at the experimental endpoint (Day 16 mean tumor volume: 439.7 vs. 732.9 mm^3, adjusted $p = 0.0155$). Notably, concurrent administration of the MCT4 inhibitor MSC-4381 further reduced the mean tumor volume to 149.1 mm^3. Pairwise comparisons revealed that this combined regimen achieved significantly enhanced antitumor efficacy relative to anti-PD-1 monotherapy alone (adjusted $p = 0.0132$, two-way RM ANOVA with Tukey's post-hoc test; Figure 5c). These data quantitatively demonstrate that MCT4 inhibition can increase the sensitivity of ccRCC to PD-1 blockade.

Mechanistically, the *SLC16A3* product MCT4 functions as a plasma-membrane lactate exporter. Its activity elevates pericellular lactate, which polarizes TAMs toward the immunosuppressive M2 phenotype and engages the lactate receptor GPR81 on tumor cells in an autocrine manner. GPR81 signaling through the ERK–c-MYC axis reprograms cancer cell metabolism, locking ccRCC cells into a highly glycolytic state and sustaining immune-refractory tumor growth. These findings support further exploration of combined MCT4 inhibition and ICB as a therapeutic strategy in ccRCC.

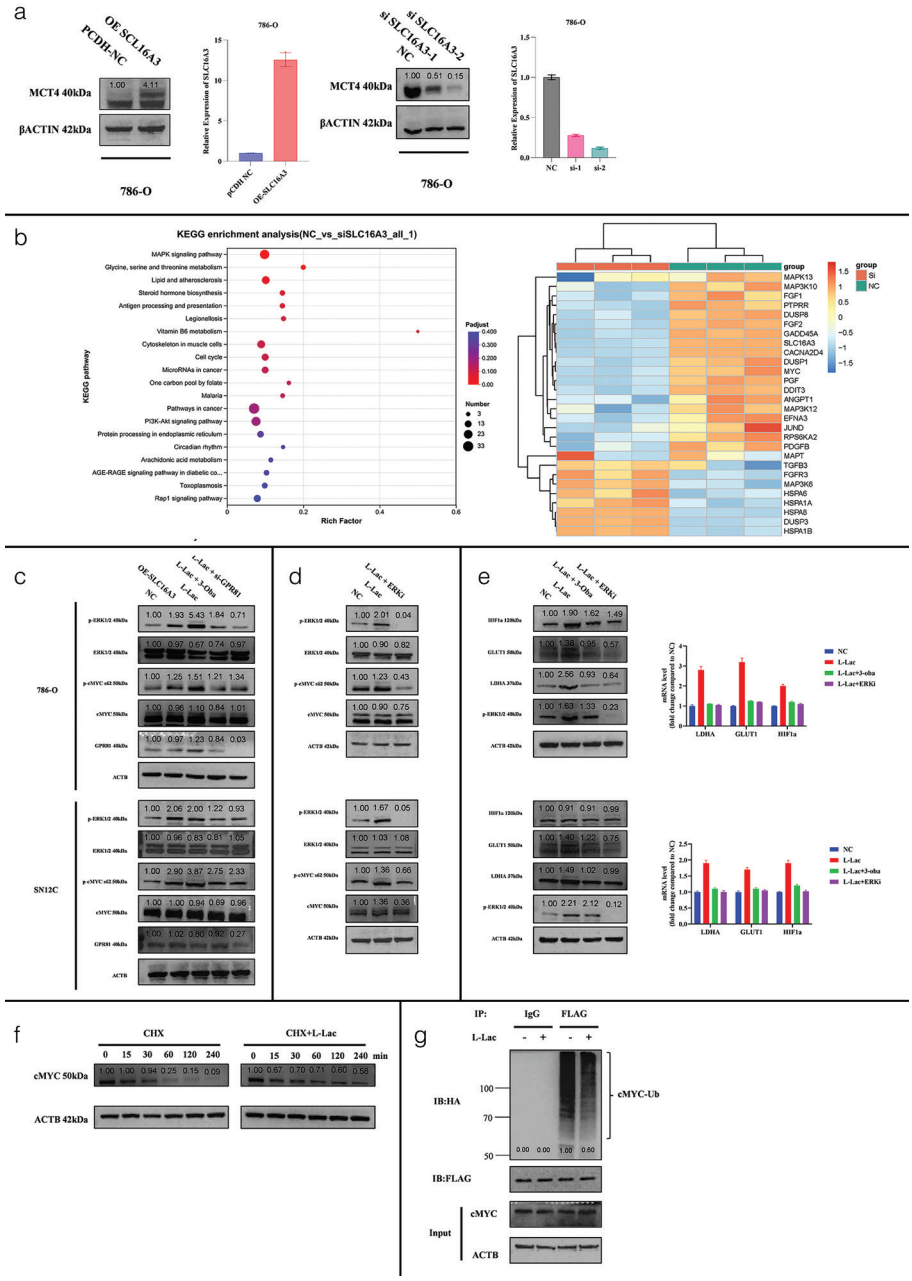

FIG. 4. Solute carrier family 16 member 3 (*SLC16A3*)-mediated lactate efflux sustains glycolysis via autocrine extracellular signal-regulated kinase (ERK)-c-MYC signaling. MCT4 protein expression in 786-O cells transfected with *SLC16A3*-overexpressing plasmid or *SLC16A3*-specific siRNA (a); RNAseq sequencing of si*SLC16A3*-mediated inhibition of the MAPK pathway in 786-O cells (b); western blot analysis evaluating the activation of the ERK-c-MYC signaling pathway in 786-O and SN12C cells following *SLC16A3* overexpression or exogenous L-lactate treatment. The abrogation of this activation by GPR81 pharmacological inhibition (3-OBA) or genetic silencing (siGPR81) is also shown (c); western blot analysis demonstrating the suppression of lactate-induced ERK-c-MYC pathway activation in 786-O and SN12C cells following treatment with an ERK inhibitor (ERKi) (d); evaluation of downstream glycolytic targets. Protein expression levels (western blot) and relative mRNA expression levels of c-MYC-dependent target genes [glucose transporter 1 (GLUT1), hypoxia-inducible factor 1 alpha (HIF1A), and lactate dehydrogenase A (LDHA)] in 786-O and SN12C cells treated with L-lactate, with or without ERKi or 3-OBA. For quantitative densitometry analysis, specific protein levels were normalized to the ACTIN internal control, and phosphorylated protein levels were normalized to their respective total protein levels (e); evaluation of c-MYC protein stability. 786-O cells were treated with the protein synthesis inhibitor cycloheximide in the presence or absence of exogenous L-lactate. c-MYC protein levels were tracked over the indicated time course via Western blot to determine its half-life (f); assessment of c-MYC ubiquitination. 786-O cells were treated with exogenous L-lactate, and the ubiquitination status of the c-MYC protein was determined by immunoprecipitation (IP) followed by western blot analysis (g). siRNA, small interfering RNA; OE, overexpression.

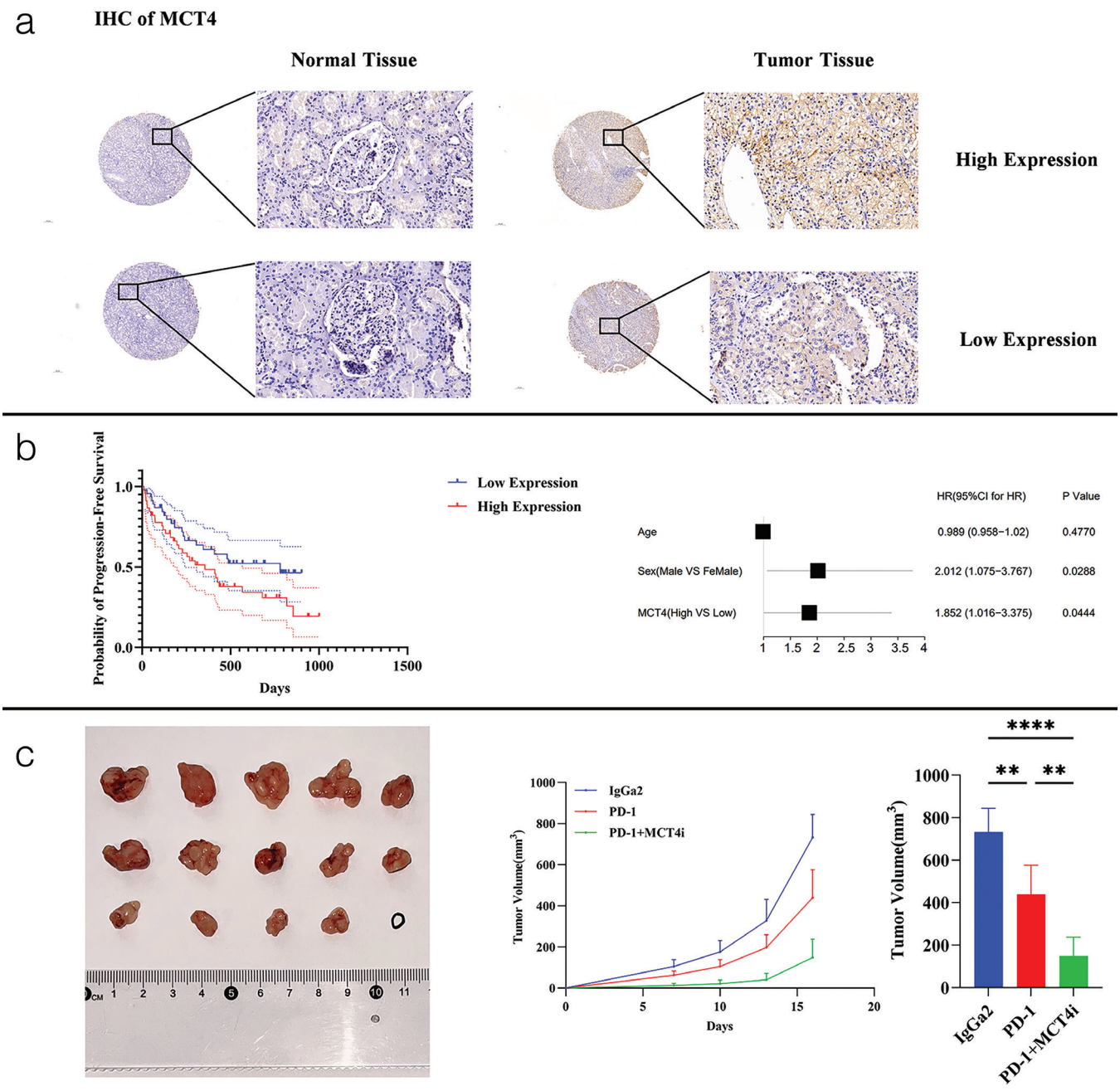

FIG. 5. Monocarboxylate transporter 4 (MCT4) inhibition enhances the antitumor effect of programmed cell death protein-1 (PD-1) blockade. Representative immunohistochemistry (IHC) staining images of MCT4 in a locally recruited tissue microarray (TMA) cohort of advanced clear cell renal cell carcinoma (ccRCC), illustrating typical cases of high and low MCT4 expression (a); Kaplan–Meier curves of progression-free survival (PFS) for the advanced ccRCC TMA cohort (n = 91 patients, 41 events), stratified into high (n = 45) and low (n = 46) MCT4 expression groups based on the median cut-off of the IHC staining index. The accompanying forest plot summarizes the multivariate Cox proportional hazards regression analysis, showing the hazard ratios (HRs) and 95% confidence intervals (CIs) for MCT4 (solute carrier family 16 member 3) expression, adjusted for clinical covariates including age (HR = 0.989, 95% CI = 0.958–1.020, $p = 0.4770$) and sex (HR = 2.012, 95% CI = 1.075–3.767, $p = 0.0288$). The analysis demonstrates that high MCT4 expression serves as an independent risk factor for worse PFS (HR = 1.852, 95% CI = 1.016–3.375, $p = 0.0444$) (b); in the subcutaneous tumor formation experiment in BALB/c mice, combined MCT4i and anti-PD-1 therapy significantly blunted tumor growth compared to anti-PD-1 monotherapy. Statistical significance for longitudinal tumor volumes was determined using two-way repeated-measures analysis of variance with Time and Treatment Group as factors, followed by Tukey's multiple comparisons test (n = 5 per group) (c). IgG2a, immunoglobulin G2a, MCT4i, MCT4 inhibitor.

DISCUSSION

ccRCC is a highly prevalent urological malignancy worldwide, accounting for approximately 2–3% of all adult cancers, with a steadily increasing annual incidence.[1] Epidemiological data from 2022 indicate that China reported nearly 77,000 new cases and 46,000 deaths related to ccRCC.[2] Current first-line treatment regimens, primarily combining tyrosine kinase inhibitors with PD-1 blockade, have extended median overall survival to beyond 30 months.[28] However, therapeutic efficacy remains substantially limited by both intrinsic and acquired resistance: approximately 30–40% of patients exhibit primary refractoriness, and nearly 70% eventually develop secondary resistance.[29] Therefore, overcoming immune evasion and addressing immunotherapy resistance remain critical priorities in the clinical management of RCC.

Recent studies have identified metabolic reprogramming within the TME as a key mechanism underlying immunotherapy failure. This metabolic rewiring involves multiple interconnected pathways, including the tryptophan–kynurenine,[30] lactate–acidosis,[31] lipid–ferroptosis,[32] and arginine–nitric oxide[33] axes, which collectively contribute to therapeutic resistance. Functionally, these dysregulated metabolic processes impair the infiltration and cytotoxic activity of effector T-cells, promote the accumulation of immunosuppressive populations such as Tregs and MDSCs, and enhance PD-L1 stabilization. Together, these mechanisms establish a highly immunosuppressive and therapy-resistant microenvironment.

Current paradigms conceptualize the TME as an integrated metabolic and immunological network. Within this context, glycolytic activity and lactate accumulation extend beyond their traditional roles in cellular bioenergetics and act as key intercellular signaling mediators that facilitate immune evasion.[34-36] Multi-omics approaches, including integrative metabolomics and single-cell transcriptomics, have demonstrated a strong positive correlation between elevated intratumoral lactate levels and increased infiltration of immunosuppressive cells, particularly Tregs, MDSCs, and TAMs. These findings position lactate as a major driver of immune privilege.[37-39] Mechanistically, lactate-mediated immunosuppression occurs through two primary pathways. First, lactate serves as a substrate for PD-L1 lactylation; pharmacological or genetic inhibition of this post-translational modification reduces PD-1 interactions and restores the cytotoxic function of $CD8^+$ T-cells.[40] Second, extracellular acidification caused by lactate accumulation suppresses mechanistic target of rapamycin complex 1 signaling and inhibits the nuclear translocation of nuclear factor of activated T-cells. This inhibition reduces proliferation, cytokine production, and granzyme release in natural killer cells and effector T-cells, while promoting macrophage polarization toward the pro-tumorigenic M2 phenotype, thereby establishing a self-reinforcing cycle of immune suppression.[24]

It is important to note that high glycolytic activity and lactate-mediated immunosuppression are hallmarks of the classical Warburg effect and occur broadly across solid tumors, rather than being specific to ccRCC. Nevertheless, therapeutic targeting of this axis holds unique and disproportionately high translational value in ccRCC. Due to canonical loss-of-function mutations in the VHL tumor suppressor gene and consequent constitutive stabilization of HIF pathways, ccRCC exhibits an intrinsic, extreme dependence on aerobic glycolysis compared with other malignancies. This metabolic wiring renders ccRCC highly reliant on efficient lactate efflux mechanisms, such as those mediated by *SLC16A3*, to prevent lethal intracellular acidification. Thus, intercepting this lactate–immune axis in a cancer type so fundamentally addicted to glycolysis represents a highly specific and actionable therapeutic vulnerability.

CRISPR *in vivo* screening simultaneously exposes the genome to native hypoxia, immune surveillance, and metabolic stress, allowing quantification of each gene's contribution to tumor fitness in a setting closely resembling the clinical environment.[41] This approach provides an efficient pathway for identifying "druggable" targets. However, the complexity of the intact host, coupled with stringent T-cell-number constraints, has limited most studies to *in vitro* bench-scale experiments. By performing a genome-wide CRISPR knockout screen in immunocompetent mice, we enriched sgRNAs targeting *SLC16A3* and other glycolytic/lactate-handling genes, highlighting the lactate–immune-evasion axis as our mechanistic priority.

The human *SLC16A3* gene is located on the long arm of chromosome 17 (17q25.3).[42] Its encoded protein, MCT4, mediates the transport of ketone bodies, pyruvate, and lactate, and is expressed in most tissues. Elevated tumor lactate levels have been significantly associated with metastasis, tumor recurrence, and poor prognosis.[25] *SLC16A3* contributes to the initiation and progression of malignancies through MCT4, which specifically facilitates lactate extrusion from cells.

Analysis using the TIMER database revealed a positive correlation between *SLC16A3* expression and M2 macrophage infiltration within the TME. Functionally, *SLC16A3* primarily modulates tumor immune regulation rather than intrinsic cell proliferation in RCC. Supporting this, Yu et al.[25] reported that *SLC16A3* may serve as a potential target to reverse tumor resistance to immunotherapy.

By systematically comparing tumor growth kinetics across *in vitro* culture, immunodeficient hosts, and immunocompetent models, our study delineates the multidimensional role of *SLC16A3* in ccRCC progression. First, at the tumor-intrinsic level, *SLC16A3* depletion induced only a marginal TGI of 16.53% in nude mice, suggesting that ccRCC cells can largely metabolically compensate for MCT4 loss to maintain autonomous proliferation. Second, in the basic immunocompetent microenvironment, the presence of a complete host immune system slightly increased the growth-inhibitory effect of *SLC16A3* depletion (TGI 18.54%), implying the initiation of microenvironmental remodeling; nevertheless, this effect remained statistically non-significant after stringent multiple-comparison adjustments. Third, and most importantly, the predominant functional impact of *SLC16A3* emerged during immune checkpoint intervention. OE of *SLC16A3* completely abolished the antitumor efficacy of PD-1 blockade, whereas its genetic ablation enhanced anti-PD-1 therapy, driving absolute TGI to 84.14%. These definitive *in vivo* data establish that the primary pathophysiological role of the *SLC16A3*–lactate axis in ccRCC is not to sustain baseline cell proliferation but to construct an immunosuppressive niche that dictates sensitivity to immune checkpoint inhibitors.

Emerging evidence indicates that tumors exploit macrophage checkpoints to orchestrate immune escape, with TAMs, particularly those polarized toward the M2 phenotype, serving as central mediators of therapeutic resistance.[43] Rather than supporting T-cell activity, M2-TAMs deploy inhibitory ligands (e.g., PD-L1, CD206, interleukin-10, and transforming growth factor beta) and metabolic cues (e.g., lactate and arginase-1) that suppress cytotoxic lymphocyte recruitment and function.[44] Consequently, contemporary immunotherapeutic strategies are shifting from sole T-cell reinvigoration toward reprogramming the macrophage checkpoint milieu, aiming to convert M2 dominance into an immunostimulatory M1 state and thereby restore effective antitumor immunity.[45]

Our investigations in ccRCC corroborate established paradigms and further reveal an autocrine circuitry in which tumor-derived lactate rewires its own glycolytic program. We demonstrated that exported lactate activates the cognate GPR81 receptor expressed on ccRCC cells, triggering an ERK phosphorylation cascade. Phosphorylated ERK subsequently phosphorylates c-MYC at Ser62, thereby preventing glycogen synthase kinase-3β–mediated phosphorylation at Thr58. This modification blocks recognition by the FBW7 ubiquitin ligase, inhibiting polyubiquitylation and proteasomal degradation of c-MYC and allowing its transcriptional activity to persist. Consequently, c-MYC drives the expression of multiple glycolytic genes, establishing a feed-forward loop that sustains high lactate output.

Interestingly, the amplitude of the lactate–GPR81–c-MYC–HIF1α axis is fundamentally dependent on the functional status of the VHL tumor suppressor. In VHL-wild-type SN12C cells, intact VHL mediates constitutive ubiquitination and rapid proteasomal degradation of HIF1α, limiting its intracellular accumulation even when c-MYC transcriptional activity is enhanced by autocrine lactate. Conversely, in VHL-null 786-O cells, which represent the canonical genetic background of most ccRCC cases, the absence of VHL-mediated degradation allows robust stabilization of HIF1α following c-MYC-driven transcription. This mechanistic interplay indicates that VHL mutational status significantly amplifies the glycolytic gain-of-function conferred by lactate self-signaling, effectively creating a hyperactive, self-sustaining MCT4–lactate feed-forward loop in VHL-deficient ccRCC. These distinct metabolic dynamics underscore the importance of considering VHL status when stratifying patients for therapies targeting lactate-dependent metabolic–immune circuits.

Patient-acquired resistance to ICB is the clinical challenge motivating this study. We therefore investigated whether *SLC16A3*, which encodes the lactate exporter MCT4, could serve as a sensitizing or resistance-reversing co-target for PD-1 therapy. In immunocompetent ccRCC models, genetic or pharmacologic blockade of MCT4 (MCT4i) combined with anti-PD-1 therapy produced deeper tumor regression than either agent alone, formally validating the translational potential of this metabolic–immune combinatorial strategy.

Our *in vivo* efficacy study highlights the clinical relevance of dual MCT4 and PD-1 blockade. While the combination group exhibited a statistically significant reduction in tumor burden compared to anti-PD-1 monotherapy, the absence of a distinct MCT4i monotherapy cohort precludes formal calculation of quantitative synergy models (e.g., Bliss independence). Therefore, rather than claiming pharmacological synergy, our data robustly support an enhanced or additive therapeutic benefit when combining an MCT4 inhibitor with ICB. This combinatorial enhancement provides a compelling rationale for further clinical investigation.

Importantly, MCT4 inhibition has advanced beyond preclinical proof-of-concept. Early-phase trials of oral MCT4 inhibitors in ccRCC patients progressing after PD-1/PD-L1 blockade are already underway and have demonstrated preliminary safety and target engagement, offering an immediate clinical scaffold for translating *SLC16A3* blockade into a strategy to overcome PD-1 resistance.

In summary, a metabolism-focused CRISPR *in vivo* screen identified *SLC16A3* as a critical driver of anti-PD-1 resistance in ccRCC. By exporting lactate, *SLC16A3* activates an autocrine GPR81–MAPK–c-MYC loop that sustains high glycolysis in tumor cells, while simultaneously promoting TAM polarization toward an immunosuppressive M2 phenotype. Pharmacologic blockade of this single transporter therefore dual-targets immune escape and metabolic fitness, cooperatively enhancing PD-1 inhibitor efficacy in immunocompetent models and establishing *SLC16A3* as a readily druggable node for reversing lactate-mediated immunotherapy resistance.

Several limitations of this study warrant consideration. First, the *in vivo* CRISPR screen was constrained by a small sample size ($n = 3$). The low lentiviral permissiveness of RENCA cells necessitated the use of a large cellular inoculum per mouse to maintain library coverage while minimizing *in vitro* clonal drift. Although MAGeCK's negative binomial model was applied to account for overdispersion, this screen primarily functioned as a hypothesis-generating platform. Accordingly, our definitive mechanistic and therapeutic conclusions are based on subsequent, adequately powered *in vivo* validation cohorts ($n \geq 5$).

Second, immune profiling in this study primarily relied on the immortalized RAW264.7 macrophage cell line and selected phenotypic markers (e.g., granzyme B, TIM-3, and LAG-3). Comprehensive functional validation of this immunometabolic axis will require future studies incorporating *in vivo* macrophage depletion models, primary bone marrow–derived macrophages, and direct $CD8^+$ T-cell functional assays, including intracellular interferon-γ production and cytotoxicity measurements.

Third, the synchronized tumor harvest required for concurrent microenvironmental profiling precluded the generation of long-term survival data. In addition, technical limitations in establishing stable *in vivo* tumor-specific Gpr81 knockout models restricted mechanistic investigations primarily to *in vitro* genetic interference and pharmacological inhibition. Consequently, the potential contribution of host-derived GPR81 (e.g., from endogenous macrophages) to the observed immunometabolic phenotypes cannot be definitively excluded.

Fourth, the *in vivo* combination therapy design lacked an independent MCT4 inhibitor monotherapy cohort, preventing formal evaluation using quantitative synergy models (e.g., Bliss independence). Therefore, the observed combinatorial effects

are conservatively interpreted as enhanced or additive efficacy rather than true pharmacological synergy. Comprehensive survival analyses and rigorous synergy modeling remain priorities for future fully powered studies.

Finally, the murine RENCA syngeneic model lacks the canonical VHL mutation characteristic of most human ccRCC cases. Nevertheless, *SLC16A3* emerged as a top resistance-associated hit in this model and demonstrated a strong correlation with M2 macrophage infiltration in clinical ccRCC datasets, supporting its continued investigation as a therapeutic target.

Ethics Committee Approval: The protocol was approved by the Ethics Committee of The Fifth Medical Center of Chinese People's Liberation Army General Hospital (approval number: KY-2022-6-40-1, date: 16.06.2022).

Informed Consent: Written informed consent permitting the future use of surplus biological material and anonymized clinical information for research purposes was obtained from each participant.

Data Sharing Statement: The data that support the findings of this study are available from the corresponding author upon reasonable request.

Authorship Contributions: Concept- S.Z., L.C.; Design- S.Z., L.C.; Supervision- L.C.; Funding- L.C.; Materials- S.Z., J.D., Y.D., C.F., X.L., B.Z., L.W., Y.Z., L.K., T.Y.; Data Collection or Processing- S.Z., J.D., Y.D., C.F., X.L., B.Z., L.W., Y.Z., L.K., T.Y.; Analysis and/or Interpretation- J.D., Y.D., C.F., X.L., B.Z., L.W., Y.Z., L.K., T.Y.; Writing- S.Z.; Critical Review- L.C.

Conflict of Interest: The authors declare that they have no conflict of interest.

Funding: This work was supported by the General Program of the National Natural Science Foundation of China (grant no: 82173085).

REFERENCES

1. Bray F, Laversanne M, Sung H, et al. Global cancer statistics 2022: GLOBOCAN estimates of incidence and mortality worldwide for 36 cancers in 185 countries. *CA Cancer J Clin*. 2024;74:229-263. [CrossRef]
2. Chinese Expert Consensus on The Systemic Treatment of Advanced Clear Cell Renal Cell Carcinoma Workgroup; Chinese Society of Clinical Oncology, Experts Committee on Renal Carcinoma; China Anti-Cancer Association, The Society of Genitourinary Tract Cancer. [Chinese expert consensus on the systemic treatment of advanced clear cell renal cell carcinoma (2024 edition)]. *Zhonghua Zhong Liu Za Zhi*. 2024;46:844-854. [CrossRef]
3. Bex A, Ghanem YA, Albiges L, et al. European Association of Urology Guidelines on Renal Cell Carcinoma: the 2025 Update. *Eur Urol*. 2025;87:683-696. [CrossRef]
4. Motzer RJ, Jonasch E, Agarwal N, et al. Kidney Cancer, Version 3.2022, NCCN Clinical Practice Guidelines in Oncology. *J Natl Compr Canc Netw*. 2022;20:71-90. [CrossRef]
5. Kopp RM, Massari F, Grande E, et al. Real-world evidences on adjuvant pembrolizumab for renal cell carcinoma: results from the multicenter real-world ARON-1 study. *Cancer Immunol Immunother*. 2025;74:374. [CrossRef]
6. Burgers FH, van der Mijn JCK, Seijkens TTP, Jedema I, Bex A, Haanen JBAG. Immunological features of clear-cell renal-cell carcinoma and resistance to immune checkpoint inhibitors. *Nat Rev Nephrol*. 2025;21:687-701. [CrossRef]
7. Anderson KG, Braun DA, Buqué A, et al. Leveraging immune resistance archetypes in solid cancer to inform next-generation anticancer therapies. *J Immunother Cancer*. 2023;11:e006533. [CrossRef]
8. Wang Y, Ma A, Song NJ, et al. Proteotoxic stress response drives T cell exhaustion and immune evasion. *Nature*. 2025;647:1025-1035. [CrossRef]
9. Al Bakir M, Reading JL, Gamble S, et al. Clonal driver neoantigen loss under EGFR TKI and immune selection pressures. *Nature*. 2025;639:1052-1059. [CrossRef]
10. Lemoine J, Ruella M, Houot R. Overcoming Intrinsic Resistance of Cancer Cells to CAR T-Cell Killing. *Clin Cancer Res*. 2021;27:6298-6306. [CrossRef]
11. Tufail M, Jiang CH, Li N. Immune evasion in cancer: mechanisms and cutting-edge therapeutic approaches. *Signal Transduct Target Ther*. 2025;10:227. [CrossRef]
12. Han Y, Zhang L, Sun D, et al. Spatiotemporal analyses of the pan-cancer single-cell landscape reveal widespread profibrotic ecotypes associated with tumor immunity. *Nat Cancer*. 2025;6:1880-1898. [CrossRef]
13. Jinek M, Chylinski K, Fonfara I, Hauer M, Doudna JA, Charpentier E. A programmable dual-RNA-guided DNA endonuclease in adaptive bacterial immunity. *Science*. 2012;337:816-821. [CrossRef]
14. Shalem O, Sanjana NE, Hartenian E, et al. Genome-scale CRISPR-Cas9 knockout screening in human cells. *Science*. 2014;343:84-87. [CrossRef]
15. Li D, Cao F, Cheng W, Xu Y, Yang C. Predictive value of estimated pulse wave velocity for cardiovascular and all-cause mortality in individuals with obesity. *Diabetol Metab Syndr*. 2023;15:40. [CrossRef]
16. Uijttewaal ECH, Lee J, Sell AC, et al. CRISPR-StAR enables high-resolution genetic screening in complex in vivo models. *Nat Biotechnol*. 2025;43:1848-1860. [CrossRef]
17. Braun CJ, Adames AC, Saur D, Rad R. Tutorial: design and execution of CRISPR in vivo screens. *Nat Protoc*. 2022;17:1903-1925. [CrossRef]
18. Cai J, Zhang P, Cai Y, et al. Lactylation-Driven NUPR1 Promotes Immunosuppression of Tumor-Infiltrating Macrophages in Hepatocellular Carcinoma. *Adv Sci (Weinh)*. 2025;12:e2413095. [CrossRef]
19. Dai J, Lu X, Zhang C, et al. NNMT promotes acquired EGFR-TKI resistance by forming EGR1 and lactate-mediated double positive feedback loops in non-small cell lung cancer. *Mol Cancer*. 2025;24:79. [CrossRef]
20. Colegio OR, Chu NQ, Szabo AL, et al. Functional polarization of tumour-associated macrophages by tumour-derived lactic acid. *Nature*. 2014;513:559-563. [CrossRef]
21. Angelin A, Gil-de-Gómez L, Dahiya S, et al. Foxp3 reprograms T cell metabolism to function in low-glucose, high-lactate environments. *Cell Metab*. 2017;25:1282-1293.e7. [CrossRef]
22. Galetin A, Brouwer KLR, Tweedie D, et al. Membrane transporters in drug development and as determinants of precision medicine. *Nat Rev Drug Discov*. 2024;23:255-280. [CrossRef]
23. Babl N, Decking SM, Voll F, et al. MCT4 blockade increases the efficacy of immune checkpoint blockade. *J Immunother Cancer*. 2023;11:e007349. [CrossRef]
24. Qian Y, Galan-Cobo A, Guijarro I, et al. MCT4-dependent lactate secretion suppresses antitumor immunity in LKB1-deficient lung adenocarcinoma. *Cancer Cell*. 2023;41:1363-1380.e7. [CrossRef]
25. Yu T, Liu Z, Tao Q, et al. Targeting tumor-intrinsic SLC16A3 to enhance anti-PD-1 efficacy via tumor immune microenvironment reprogramming. *Cancer Lett*. 2024;589:216824. [CrossRef]
26. Pu Z, Sui B, Wang X, Wang W, Li L, Xie H. The effects and mechanisms of the anti-COVID-19 traditional Chinese medicine, Dehydroandrographolide from Andrographis paniculata (Burm.f.) Wall, on acute lung injury by the inhibition of NLRP3-mediated pyroptosis. *Phytomedicine*. 2023;114:154753. [CrossRef]
27. Tsai WB, Aiba I, Long Y, Lin HK, Feun L, Savaraj N, Kuo MT. Activation of Ras/PI3K/ERK pathway induces c-Myc stabilization to upregulate argininosuccinate synthetase, leading to arginine deiminase resistance in melanoma cells. *Cancer Res*. 2012;72:2622-2633. [CrossRef]
28. Rini BI, Plimack ER, Stus V, et al. Pembrolizumab plus axitinib versus sunitinib for advanced renal-cell carcinoma. *N Engl J Med*. 2019;380:1116-1127. [CrossRef]
29. Au L, Hatipoglu E, Robert de Massy M, et al. Determinants of anti-PD-1 response and resistance in clear cell renal cell carcinoma. *Cancer Cell*. 2021;39:1497-1518.e11. [CrossRef]
30. Li H, Bullock K, Gurjao C, et al. Metabolomic adaptations and correlates of survival to immune checkpoint blockade. *Nat Commun*. 2019;10:4346. [CrossRef]
31. Watson MJ, Vignali PDA, Mullett SJ, et al. Metabolic support of tumour-infiltrating regulatory T cells by lactic acid. *Nature*. 2021;591:645-651. [CrossRef]
32. Kim R, Taylor D, Vonderheide RH, Gabrilovich DI. Ferroptosis of immune cells in the tumor microenvironment. *Trends Pharmacol Sci*. 2023;44:542-552. [CrossRef]
33. Canè S, Geiger R, Bronte V. The roles of arginases and arginine in immunity. *Nat Rev Immunol*. 2025;25:266-284. [CrossRef]
34. Wang ZH, Peng WB, Zhang P, Yang XP, Zhou Q. Lactate in the tumour microenvironment: From immune modulation to therapy. *EBioMedicine*. 2021;73:103627. [CrossRef]
35. Xu N, Zhu Y, Han Y, et al. Targeting MondoA-TXNIP restores antitumour immunity in lactic-acid-induced immunosuppressive microenvironment. *Nat Metab*. 2025;7:1889-1904. [CrossRef]
36. Yang J, Yu X, Xiao M, et al. Histone lactylation-driven feedback loop modulates cholesterol-linked immunosuppression in pancreatic cancer. *Gut*. 2025;74:1859-1872. [CrossRef]

37. Sun K, Zhang X, Shi J, et al. Elevated protein lactylation promotes immunosuppressive microenvironment and therapeutic resistance in pancreatic ductal adenocarcinoma. *J Clin Invest.* 2025;135:e187024. [CrossRef]
38. Xue Q, Peng W, Zhang S, et al. Lactylation-driven TNFR2 expression in regulatory T cells promotes the progression of malignant pleural effusion. *J Immunother Cancer.* 2024;12:e010040. [CrossRef]
39. Shen L, Wang S, Gao C, et al. Tumour-associated macrophages serve as an acetate reservoir to drive hepatocellular carcinoma metastasis. *Nat Metab.* 2025;7:2268-2283. [CrossRef]
40. Tong H, Jiang Z, Song L, et al. Dual impacts of serine/glycine-free diet in enhancing antitumor immunity and promoting evasion via PD-L1 lactylation. *Cell Metab.* 2024;36:2493-2510.e9. [CrossRef]
41. Biederstädt A, Basar R, Park JM, et al. Genome-wide CRISPR screens identify critical targets to enhance CAR-NK cell antitumor potency. *Cancer Cell.* 2025;43:2069-2088.e11. [CrossRef]
42. Tao Q, Li X, Zhu T, et al. Lactate transporter SLC16A3 (MCT4) as an onco-immunological biomarker associating tumor microenvironment and immune responses in lung cancer. *Int J Gen Med.* 2022;15:4465-4474. [CrossRef]
43. Wang H, Yu H, Bai X, et al. Recent advances in hydrogel-based delivery systems for the treatment of pancreatic cancer. *Mater Today Bio.* 2025;35:102487. [CrossRef]
44. Helal IM, Kamal MA, Abd El-Aziz MK, El Tayebi HM. Epigenetic tuning of tumour-associated macrophages (TAMs): a potential approach in hepatocellular carcinoma (HCC) immunotherapy. *Expert Rev Mol Med.* 2024;26:e18. [CrossRef]
45. Chen D, Xie J, Fiskesund R, et al. Publisher correction: chloroquine modulates antitumor immune response by resetting tumor-associated macrophages toward M1 phenotype. *Nat Commun.* 2018;9:1808. [CrossRef]